Article

Patterns

Mechanical improvement of boron nitride nanosheet-reinforced cement paste by multiscale modeling

Graphical abstract

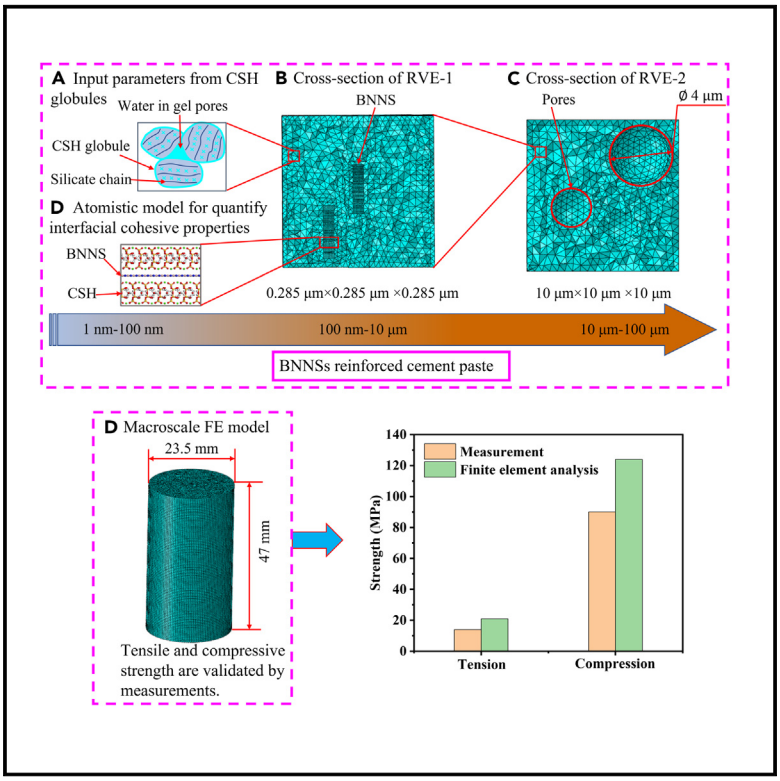

Highlights

- The multiscale modeling is constructed to mimic BNNS-reinforced cement paste
- The micropores and BNNSs are explicitly considered in the RVE models
- MD-based cohesive zone model describes the interface between BNNSs and cement paste
- Predictions of tensile and compressive strength are close to measurements

Authors

Jialin Liu, Weihe Liu, Cheuk Lun Chow, Denvid Lau

Correspondence

denvid.lau@cityu.edu.hk

In brief

There is a gap between the mechanical improvement of boron nitride nanosheets in calcium silicate hydrates and the mechanical properties of macroscale samples. To link the material properties of the nanoscale cementitious composites to the tensile strength and compressive strength of the macroscale samples, multiscale simulations are performed, which give a comprehensive evaluation of the mechanical improvement of boron nitride nanosheet-reinforced cementitious composites by molecular dynamics simulations and finite-element analysis.

Liu et al., 2023, Patterns *4*, 100724
May 12, 2023
https://doi.org/10.1016/j.patter.2023.100724

CellPress

Patterns

CellPress
OPEN ACCESS

Article

Mechanical improvement of boron nitride nanosheet-reinforced cement paste by multiscale modeling

Jialin Liu,[1] Weihe Liu,[2] Cheuk Lun Chow,[1] and Denvid Lau[1,3,*]
[1]Department of Architecture and Civil Engineering, City University of Hong Kong, Hong Kong, China
[2]Department of Civil and Environmental Engineering, The Hong Kong Polytechnic University, Hong Kong, China
[3]Lead contact
*Correspondence: denvid.lau@cityu.edu.hk
https://doi.org/10.1016/j.patter.2023.100724

THE BIGGER PICTURE Boron nitride nanosheets (BNNSs) show excellent improvement in the mechanical properties of cementitious composites at the nanoscale, which is a promising reinforcement for the structural performance of engineering structures. In view of BNNSs being expensive, it is necessary to provide a guideline for manufacturing BNNS-reinforced cementitious composites so that we can obtain the expected mechanical improvement in the structural performance of engineering structures. To link the material properties of the nanocomposites to the macroscale mechanical performance of engineering structures, multiscale models are constructed to describe BNNS-reinforced cement paste from the microscale to the macroscale. The mechanical properties of two-dimensional nanomaterial-reinforced cementitious composites can be accurately predicted by finite-element analysis, which can be applied in the computer-aided design of concrete structures and can reduce the cost and waste of design of concrete structures.

Proof-of-Concept: Data science output has been formulated, implemented, and tested for one domain/problem

SUMMARY

Representative volume (RVE) models are constructed to mimic the microstructural characteristics of boron nitride nanosheet (BNNS)-reinforced cement paste. The interfacial properties between BNNSs and cement paste are described by the cohesive zone model (CZM) developed by molecular dynamics (MD) simulations. Based on the RVE models and the MD-based CZM, the mechanical properties of the macroscale cement paste are obtained by finite element analysis (FEA). To validate the accuracy of the MD-based CZM, the tensile strength and compressive strength of BNNS-reinforced cement paste from the FEA are compared with those from measurements. The FEA shows that the compressive strength of BNNS-reinforced cement paste is close to that of the measurements. The discrepancy of the tensile strength of BNNS-reinforced cement paste between the FEA and the measurements is distributed to the load transfer at the BNNS-tobermorite interface through the inclined BNNSs.

INTRODUCTION

Boron nitride nanosheets (BNNSs) are widely used as nanoreinforcement in the mechanical improvement of cementitious composites[1,2] because of their attractive mechanical properties.[3] It is reported that Young's modulus and the fracture strength of the monolayered BNNS are up to 1.3 TPa[4] and 217 GPa,[5] respectively. Compared with graphene, the robust interfacial interaction between BNNSs and cementitious composites yields a more significant improvement in the mechanical properties of cementitious composites.[1,6] The addition of a 1% weight fraction of BNNSs and graphene increases the toughness of cement paste by 85% and 10%, respectively.[2] BNNSs show better reinforcement than graphene because BNNSs have better interfacial properties with cement hydration products, which is represented by tobermorite. Specifically, the polarized boron–nitrogen bonds result in unsymmetric partial charge distribution on boron and nitrogen atoms. The partial charges yield an electrostatic

interaction between BNNSs and tobermorite,[7] which does not exist in the interface between graphene and tobermorite. Moreover, the electronegativity of the nitrogen atoms forms hydrogen bonds with the silicate chains,[8] which further improves the interfacial interaction between BNNSs and tobermorite. Hence, the load transfer at the BNNS-tobermorite interface is more robust than that at the graphene-tobermorite interface. The improvement in material properties of cementitious composites shows a promising application in reinforcing the structural performance of engineering structures. However, there is a gap between the structural performance of the macroscale engineering structures and the material properties of the nanoscale cementitious composites. To have a comprehensive evaluation of the engineering structures, linking the material properties of the nanoscale cementitious composites to the structural performance of the macroscale engineering structures is needed, which is beneficial for the design of concrete structures.

Modeling provides a guideline for improving the structural performance and enhancing the structural safety of concrete structures.[9,10] The modeling method includes atomistic modeling for describing materials from atomistic perspectives (e.g., molecular dynamics simulation) and the continuum mechanics approach for describing materials from macroscopic perspectives (e.g., FEA).[11,12] In view of the heterogeneity of BNNS-reinforced cementitious composites, the multiscale modeling covering the nanoscale materials and the macroscale materials are adopted to simultaneously describe the materials in different length scales in cementitious composites[11,13] because the properties of the heterogeneous materials are dependent on the microstructures.[14,15] To have a detailed description of the microstructure of heterogeneous materials, the representative volume element (RVE) is adopted to use the mechanical properties of a material volume to represent that of the whole heterogeneous material.[16] The RVE model transfers the structural information and mechanical properties at the nanoscale to the continuum model at the macroscale, which shows good accuracy and computational efficiency.[14,17] The RVE model of BNNS-reinforced cementitious composites contains the nanoreinforcement (i.e., BNNSs), the cementitious matrix, and the reinforcement-matrix interface. In the RVE model, the nanosheets are represented by the equivalent shell to accurately describes the mechanical performance of BNNSs.[11,18] To obtain the material properties of the equivalent shell, the nanosheets are discretized by a space frame-type finite element model. Previous research shows that the covalent bonds between atoms in nanostructures (e.g., graphene and BNNS) are represented by the beam elements; the spring element; the truss, rod, or frame element; the two-dimensional planar element; and the three-dimensional solid element.[17] Considering that the finite element prediction of mechanical properties of BNNSs modeled by the spring element is consistent with that obtained from the molecular theory,[19] the spring element is used to represent the covalent bonds in BNNSs through two groups of spring elements.[17,20,21] Specifically, the translations and angular variations of the covalent bonds between atoms of one hexagonal lattice are represented by six spring elements, respectively.[17,21] In the FEA of the mechanical performance of cementitious composites, various constitutive models are proposed to study the mechanical properties of cementitious composites under different loading conditions, including the empirical models, linear elastic model, non-linear elastic models, plasticity-based models, fracturing models, etc.[22] For the compressive loading, the cementitious composites are described by plasticity-based models because of the plastic deformation and damage due to the plastic slip and microcracking in cementitious composites.[23,24] The cementitious composites exhibit asymmetric strength under compressive loads and tensile loads.[25,26] Besides, the shear strength of the cementitious composites is dependent on the confinement from external normal stress or hydrostatic pressure. This cohesive-frictional behavior can be described by the Mohr-Coulomb model to predict the mechanical properties and plastic deformation behavior of cementitious composites.[27] However, the study of the interface between BNNSs and cementitious composites is limited. The interfacial cohesive properties between BNNSs and cementitious composites is significant to the interfacial load transfer and the mechanical improvement of cementitious composites.

An accurate representation of the interface between BNNSs and cementitious composites is the prerequisite for the prediction of the mechanical properties of cementitious composites in numerical simulations. The cohesive zone model is extensively used to simulate the interfacial behavior of cementitious composites in numerical simulations and shows good accuracy in predicting the compressive properties of cementitious composites with respect to the experimental results.[28,29] In the cohesive zone model, the interfacial interaction between the reinforcement and the matrix is modeled by the traction-separation relation. It is not uncommon for the experimental approach to be used to obtain the traction-separation relation for the cohesive zone model in numerical simulations,[30,31] whereas the defects at the interface between the reinforcement and the matrix can influence the interfacial fracture or debonding.[31] As a result, the measured traction-separation relation is dependent on the geometric characteristics (e.g., the number and the shape) of the interfacial defects. The measurements can be scattered. Molecular dynamics (MD) simulation is a promising alternative that can be used to obtain the traction-separation relation at the interface between the reinforcement and the matrix from the atomistic perspective because the defects at the interface between BNNSs and crystalline cementitious structures can be removed in MD simulations. Previous research exhibits proper accuracy in predicting the mechanical properties of composites by using the MD-based cohesive zone model with respect to experimental results.[32–35] The verified MD-based cohesive zone model ensures that the mechanical properties of BNNS-reinforced cementitious composites can be accurately predicted.

This article aims to construct a multiscale model of BNNS-reinforced cement paste to predict the tensile strength and compressive strength of the composite. To describe the interfacial behavior between BNNSs and cement paste in numerical simulations, the traction-separation relation for the cohesive zone model at the interface between BNNSs and cement paste is developed by MD simulation. The MD-based cohesive zone model is adopted to represent the interface between BNNSs and cement paste in the RVE model with periodic boundary conditions. The material properties of the RVE model are obtained by performing tensile tests and compressive tests. Afterward, the

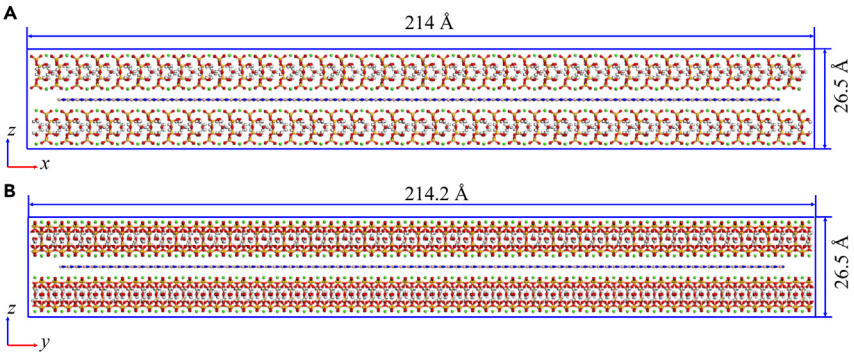

Figure 1. Atomistic model of BNNS-reinforced tobermorite
(A) The model in the *xz* plane.
(B) The model in the *yz* plane.

material properties of the RVE model are taken as the input parameters in the FEA to study the tensile and the compressive properties of the macroscale BNNS-reinforced cement paste. The porosity of the BNNS-reinforced cement paste is considered in the RVE model, which echoes the porosity of the specimen made from BNNS-reinforced cement paste in previous research. Using the RVE models can predict the tensile strength and compressive strength of the macroscale BNNS-reinforced cement paste. To validate the accuracy of the multiscale modeling of the BNNS-reinforced cement paste, the tensile strength and compressive strength of the macroscale BNNS-reinforced cement paste from the FEA are compared with the experimental results in the previous research. This study simulates the two-dimensional nanomaterial-reinforced cementitious composite by multiscale modeling and accurately predicts the tensile strength and compressive strength of the macroscale cementitious composites. The tensile strength and compressive strength of the macroscale cementitious composites are linked to the structural performance of concrete structures. As a result, the nanomaterial-reinforced concrete structures can be designed at the nanoscale to improve the structural performance at the macroscale.

Simulation program

MD-based cohesive model

Atomistic model and forcefields. Calcium silicate hydrate (CSH) is the major hydration product of Portland cement paste, occupying 70% of the hydration products. Hence, CSH is extensively used in MD simulations to represent cementitious composites. To model the major hydration product (i.e., CSH), tobermorite is constructed. The realistic model of CSH is proposed by allowing the existence of the short silicate chains (e.g., monomers, dimers, and pentamers).[36–38] This model is developed from tobermorite model. Compared with the realistic model of CSH, the tobermorite model exhibits long silicate chains without breaking. The long silicate chains of the tobermorite model can better describe the morphology of CSH on the surface of BNNSs during cement hydration products because BNNSs provide nucleation sites and yield more ordered and less spatial CSH gel on BNNSs.[39] As a result, the tobermorite model with long chains is adopted to describe the interfacial interaction between BNNSs and CSH gel in cementitious materials.[7,40] The INTERFACE forcefield is used to describe the interactions between atoms in tobermorite because the INTERFACE forcefield exhibits accurate prediction on the elastic properties of tobermorite. It is reported that the bulk modulus and Poisson's ratio of tobermorite are 71 GPa and 0.29, respectively, by using the INTERFACE forcefield in the classical MD simulations, which are close to the density functional theory (DFT) calculations of 67 GPa and 0.30, respectively.[41,42] In view of the hydration products growing on the surface of BNNSs in the hydration process, the atomistic model of BNNS-reinforced tobermorite composites is constructed by inserting BNNSs into the interlayer of tobermorite, as shown in Figure 1A in the xz plane and Figure 1B in the yz plane.

The interactions between atoms in BNNSs are described by Tersoff potential for representing the sp^2-hybridized structure of BNNS.[43–45] Due to the polarized boron–nitrogen bonds, boron atoms and nitrogen atoms exhibit partial charges. The partial charges on boron atoms and nitrogen atoms are inconsistent based on a different method. The linear combination of atomic orbitals molecular orbital method gives partial charges of 0.4 and −0.4 *e* on boron atoms and nitrogen atoms, respectively,[46] while the charges from electrostatic potentials using a grid-based method give partial charges of 1.3 and −1.3 *e* on boron atoms and nitrogen atoms, respectively.[46] In view of the partial charge of 0.4 *e* on boron atoms and the partial charge of −0.4 *e* on nitrogen atoms yielding a more stable two-dimensional nanosheet of BNNS (i.e., no severe distortion and crumpling in BNNS) than the partial charge of 1.3 *e* on boron atoms and the partial charge of −1.3 *e* on nitrogen atoms, the partial charges on boron and nitrogen atoms are 0.4 and −0.4 *e* in the MD simulation, respectively.[40] The presence of BNNS decreases the average sizes of pores in cement paste significantly, which is of benefit to improve the tensile and compressive strengths of cementitious composites. Besides, the load transfer at the BNNS-tobermorite interface impedes the development of pores in cement paste due to robust interfacial interactions between BNNS and tobermorite. The cracks are created around the pores due to stress concentration under loading. Due to the presence of BNNSs, the resistance along the crack propagation path is improved. As a result, the crack deflection occurs, showing the tortuous path of the crack in BNNS-reinforced tobermorite.[47]

To accurately describe the interfacial interaction between BNNS and tobermorite, previous research shows that the DREIDING forcefield is a good candidate.[40,48] It is reported that the MD simulation results of the tensile modulus of the BNNS-tobermorite composite are very close to the DFT calculation. Specifically, the DFT calculation shows that the tensile modulus of the BNNS-tobermorite composite is 58.3 GPa.[48] In the classical MD simulation, the BNNS-tobermorite composite with the same weight fraction of BNNSs yields a tensile modulus of 60.7 ± 1.2 GPa.[40] In the DREIDING forcefield, the non-bonded interaction is described by the electrostatic interaction E_{Coul} and

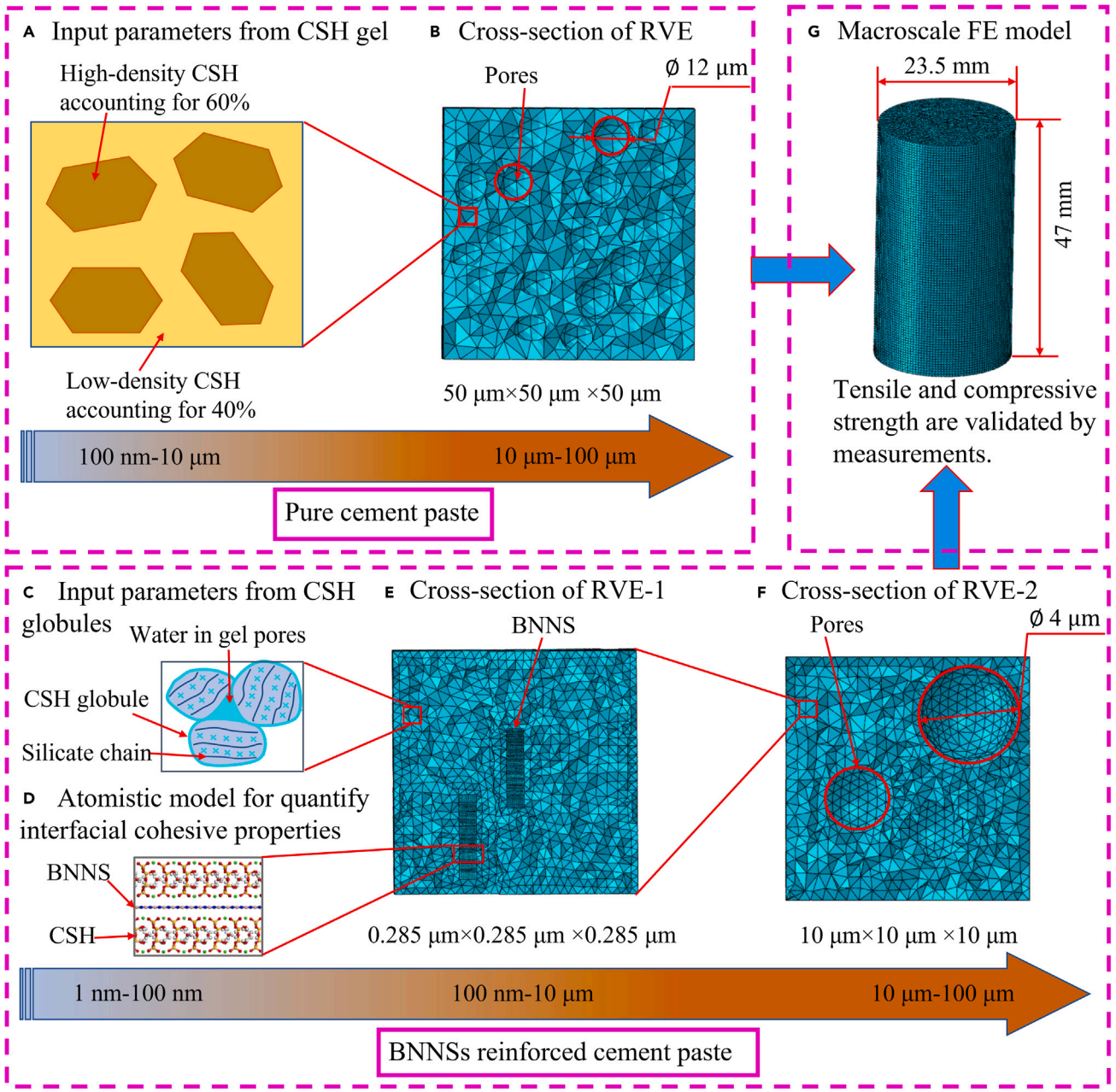

Figure 2. Multiscale modeling of pure cement paste and BNNS-reinforced cement paste

(A) The material properties of nanoscale cement paste obtained from the high-density CSH and the low-density CSH are input parameters for the RVE model.

(B) The material properties from nanoscale cement paste are invoked in the mesoscale cement paste for FEA. The cross-section of the RVE model with pores is constructed. The diameter of the pores is 12 microns, according to the mesoscale cement paste.

(C) The material properties of CSH globules are input parameters for the RVE-1 model.

(D) The interface between BNNS and CSH from the atomistic perspective.

(E) The RVE-1 model without pores yields the material properties of the cement paste, which are adopted to simulate the mechanical properties of the RVE-2 model with pores.

(F) The RVE-2 model with pores yields the material properties of the cement paste, which are adopted to simulate the mechanical properties of the macroscale cement paste sample.

(G) The multiscale modeling of pure cement paste is validated by comparing the prediction of the tensile strength and compressive strength of the macroscale cement paste sample to that of the measurements in previous research.

Table 1. Material properties of the mesoscale cement paste

Properties	Values
Young's modulus (GPa)	27[55]
Density (kg/m^3)	2,200[36,59]
Cohesion (MPa)	50[55]
Tensile strength (MPa)	66[55]
Frictional angle (°)	12[55]
Poisson's ratio	0.24[60]
Tensile fracture energy (N/m)	1.72[59,61]

van der Waals interaction E_{vdW}.[49] The hydrogen bonds are explicitly defined between nitrogen atoms in BNNS and hydrogen atoms in Si-OH, which is given by[49]

$$E_{hb} = D_{hb}\left[5(R_{hb}/R_{DA})^{12} - 6(R_{hb}/R_{DA})^{10}\right]\cos^4\theta_{DHA} \quad \text{(Equation 1)}$$

where θ_{DHA} and R_{DA} are the donor-hydrogen-acceptor angle and the donor-acceptor distance, respectively.

Shear tests and tensile test for cohesive properties. The non-bonded interaction between BNNS and tobermorite allows shear deformation-induced sliding and tensile deformation-induced peeling at the interface, which results in the deterioration of the load-transfer capacity at the interface. The corresponding interfacial cohesive properties between BNNS and tobermorite are adopted to quantify the load-transfer capacity due to sliding and peeling at the interface. To measure the interfacial cohesive properties between BNNS and tobermorite, shear tests and the tensile test are performed in the open-source code large-scale atomic/molecular massively parallel simulator (LAMMPS).[50] The tensile test is performed by loading in the z direction, as shown in Figures 1A and 1B. The shear tests are performed by loading in the xz direction and the yz direction, as shown in Figures 1A and 1B, respectively. The mechanical properties of the tobermorite-based material are significantly dependent on the strain rate in MD simulations. For example, the high strain rate results in high mechanical properties of the tobermorite-based material because the material is damaged evenly at several locations, which requires high external work to be done to overcome the interaction between atoms,[51] while the low strain rate has limited influence on the mechanical properties of tobermorite-based materials.[52,53] It is reported that the tensile strengths of pure tobermorite are 2.03 and 2.41 GPa under the tensile strain rates of 1×10^8 and 1×10^9 s^{-1}, respectively; the tensile moduli of tobermorite are 40.11 and 42.05 GPa under the tensile strain rates of 1×10^8 and 1×10^9 s^{-1}, respectively.[51] The shear moduli of the BNNS-tobermorite composite are 70.1 ± 3.7 and 73.5 ± 1.8 GPa under the shear strain rates of 1×10^8 and 1×10^9 s^{-1}, respectively.[7] In view of the insensitivity of mechanical properties of tobermorite-based materials to the low strain rate ranging from 1×10^8 to 1×10^9 s^{-1}, the strain rate of 1×10^9 s^{-1} is adopted in the shear tests and the tensile test in MD simulations. Under the strain rate of 1×10^9 s^{-1}, the effect of BNNS sizes on the cohesive properties is studied by adopting different sizes of BNNSs in the shear tests and the tensile test. By performing shear tests and the tensile test on BNNS-tobermorite composites with different sizes, the size of the BNNS-tobermorite composite is determined (discussed in MD-based traction-separation relation), and the corresponding simulation results are adopted as input parameters in the further FEA.

FEA

Validation strategy. The accurate prediction of the mechanical properties of BNNS-reinforced cement paste is dependent on the Mohr-Coulomb model for describing the mechanical behavior of pure cement paste and the MD-based cohesive zone model for describing the interface between BNNSs and cement paste. The accuracy of the Mohr-Coulomb model for predicting the mechanical properties of pure cement paste is validated first

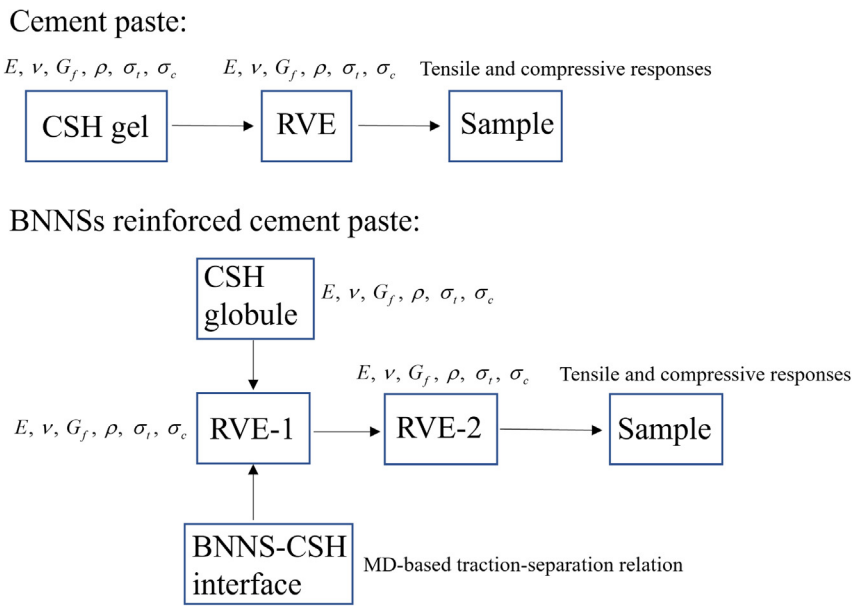

Figure 3. The flow of input parameters in multiscale models

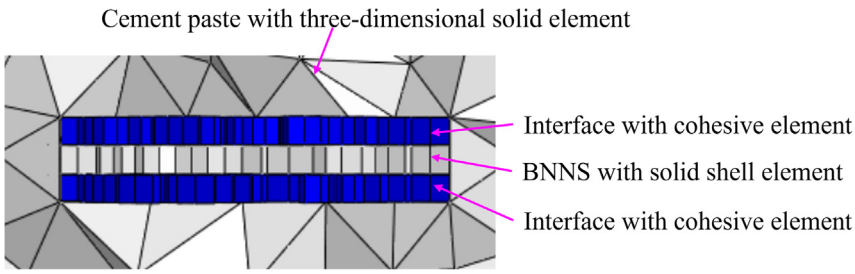

Figure 4. Description of finite element model at the interface between BNNSs and cement paste

by comparing the tensile and compressive strengths of the macroscale cement paste from the FEA with that from measurements in previous research. To validate the accuracy of the MD-based cohesive zone model for describing the interface between BNNSs and cement paste, we compare the tensile and the compressive strengths of BNNS-reinforced cement paste from the FEA with that from the measurements in previous research. The close tensile strength and compressive strength of BNNS-reinforced cement paste from the FEA and the measurements indicate that the MD-based cohesive model is appropriate for describing the interface between BNNSs and cement paste.

Multiscale models of pure cement paste. The multiscale modeling of pure cement paste covers different length scales, including the microscale cement paste consisting of the low-density and high-density CSH and the microscale pores and the macroscale cement paste, as shown in Figures 2A, 2B, and 2G, respectively. The material properties of the low-density and high-density CSH are input parameters for the cement paste in the FEA. To explicitly consider the influence of the pores on the tensile strength and compressive strength of cement paste, the pores are included in the finite element model. The average diameter of the microscale pores in pure cement paste is 12 μm, as shown in Figure 2B. The measured porosity of 22.55% is adopted in the pure cement paste. The finite element model of the macroscale cement paste can be constructed to include the microscale pores. However, it requires refining the elements around the microscale pores to a microscale size in the finite element model. The pore sizes, as shown in Figure 2B, are much smaller than that of the macroscale cement paste, as shown in Figure 2G. As a result, the element number of the cylinder specimens is so large that the FEA is computationally inefficient. To improve the computational efficiency of the FEA, the RVE model is constructed to represent the cement paste with pores at the length scale of 10–100 μm. The periodic boundary conditions are adopted on the six surfaces of the RVE model. The periodic boundary conditions require symmetric mesh on the opposite surfaces of the RVE model so that the displacements on the nodes of the opposite surfaces can be linked correctly.[54] To have symmetric mesh on the opposite sides of the RVE model, the pores are included inside the RVE model. The strain rate and the RVE sizes in the FEA are determined by adopting different levels of strain rates and RVE sizes, which are discussed in validation of Mohr-Coulomb model for cement paste. The tensile strength and compressive strength of the RVE model can be adopted to describe the macroscale cement paste in the FEA by adopting the Mohr-Coulomb model. The diameter and the height of the finite element model for representing the macroscale cement paste are 23.5 and 47 mm in Figure 2G, respectively, which echo the sizes of the cylinder specimen manufactured in previous experimental research.[1]

The Mohr-Coulomb model is reported to be appropriate for simulating cementitious composites due to its pressure-sensitive plastic behavior, as discussed in the introduction.

Although the Mohr-Coulomb model is widely used in cementitious composites, the accuracy of the material parameters of the macroscopic cement paste obtained from the multiscale modeling is required to be validated. The multiscale modeling starts from the low- and high-density CSH. The material properties of the low-density and high-density CSH are referred to in the previous multiscale investigation.[55] For the cement paste with a water/cement ratio of 0.4, the low-density and high-density CSH account for 40% and 60%, respectively.[56] Hence, Young's modulus and the density of CSH are estimated by the fraction of the low-density and high-density CSH, as shown in Table 1. The tensile strength and the cohesion of the cement paste are determined by the low-density CSH because the low-density CSH exhibits lower tensile strength and cohesion than those of the high-density CSH. Poisson's ratio and the frictional angle are identical for the low-density and high-density CSH, as shown in Table 1. Under tensile loading, the cement paste is damaged at local sites. The stress transferred at the discontinuity of the damaged location is decaying with the strain showing plastic behavior. The softening curve is adopted to simulate the plasticity of cementitious composites at the discontinuity of the damaged location, which is given by[57,58]

$$t_n = f_t \exp\left(-\frac{f_t}{G_f}\kappa\right) \quad \text{(Equation 2)}$$

where t_n is the traction force transferred across the discontinuity of the damaged location; f_t is the tensile strength; G_f is the tensile fracture energy; and κ is the largest normal separation at the damaged location.

Multiscale models of BNNS-reinforced cement paste. The multiscale models of BNNS-reinforced cement paste are different from that of the pure cement paste. In view of the sizes of pores being much larger than the sizes of BNNSs (the sizes of BNNSs in cement paste are less than 0.3 μm[1]) in cement paste, the mesh sizes around BNNSs in cement paste need to be refined to have an accurate description of the interface between BNNSs and cement paste in the finite element model. Hence, the finite element model of cement paste consists of a large number of elements, including the pores and BNNSs simultaneously. As a result, the FEA is expensive. To avoid the expensive simulation, the mesoscale cement paste is modeled by two hierarchical RVE models.

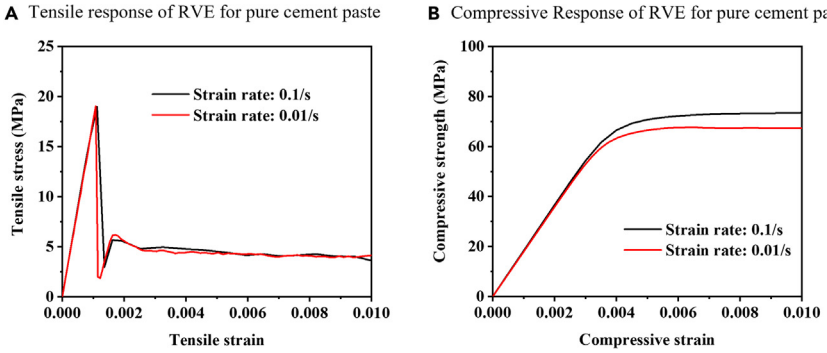

Figure 5. Mechanical responses of the RVE model for pure cement paste with a side length of 50 μm

(A) The tensile responses under the strain rates of 0.1/s and 0.01/s.

(B) The compressive responses under the the strain rates of 0.1/s and 0.01/s.

The first one is constructed to only include cement paste and BNNSs without explicit pores at the length scale of 100 nm to 1 μm, as shown in Figure 2E, denoted by RVE-1. The average size of BNNSs dispersed in cement paste is 0.1 μm.[1] The addition of BNNSs to cement paste significantly decreases the average pore sizes from 12 to 4 μm.[1] At the same time, the change in the porosity of cement paste is limited with the addition of nanosheets. For example, the porosities of the cement paste with the addition of nanosheets by weight contents of 0%, 0.02%, and 0.04% are 20.48%, 20.31%, and 20.27%, respectively. In this study, the porosity of the BNNS-reinforced cement paste is identical to that of the pure cement paste.

The material properties obtained from the RVE-1 model, including BNNSs and cement paste, are taken as the input parameters of the RVE-2 model, including the explicit pores and cement paste. The RVE-2 model of BNNS-reinforced cement paste is shown in Figure 2F. Finally, the tensile tests and compressive tests are performed on the RVE-2 model to obtain the material properties, which are taken as the input parameters of the Mohr-Coulomb model for describing the macroscale cement paste, as shown in Figure 2G. The RVE model for pure cement paste and the RVE-2 model for BNNS-reinforced cement paste represent different cementitious materials and have different material properties. Besides, the average pore sizes in the RVE model and in the RVE-2 model are 12 and 4 μm, respectively. As a result, the tensile strength and compressive strength of the RVE model for pure cement paste and the RVE-2 model for BNNS-reinforced cement paste are different. The flow of the input parameters in the multiscale model of pure cement paste and BNNS-reinforced cement paste is shown in Figure 3. BNNSs are not explicitly constructed in the homogeneous model of the macroscale cement paste in Figure 2G, but the mechanical properties of the macroscale cement paste are significantly dependent on the RVE-1 model that includes BNNSs. Hence, the homogeneous model of the macroscale cement paste is capable of characterizing the mechanical properties of BNNS-reinforced cement paste. In the RVE models for describing the BNNS-reinforced mesoscale cement paste, the RVE-2 model in Figure 2F is similar to that of pure cement paste in Figure 2B. In the RVE-1 model, the interface between BNNSs and CSH is described by cohesive zone model, as shown in Fig ure 4. It is reported that the thicknesses of BNNSs are 10 and 10–20 nm, accounting for 80% and 20%, respectively.[1] From these measurements, the average thickness of BNNSs is 7 nm. CSH exhibits higher mechanical properties than that of the interface between BNNSs and CSH. As a result, the dominant failure mode in the FEA for the RVE-1 model is interface failure, which echoes the pullout phenomenon of nanosheets in cementitious composites under external loadings.[2,62] The tensile strength and the compressive strength of the RVE-1 model are dependent on the interface failure mode. Hence, the accuracy of the interfacial cohesive properties represented by the cohesive zone model is significant.

RESULTS AND DISCUSSIONS

Validation of Mohr-Coulomb model for cement paste

The tensile strength and the compressive strength of cementitious composites are dependent on the strain rate. It is reported that the dynamic tensile and compressive strengths of cementitious composites increase rapidly when the strain rate increases from 1/s to 10^1/s.[25,63] To determine the strain rate in the FEA, strain rates of 0.1/s and 0.01/s are set to deform the RVE model with a slide length of 50 μm in the

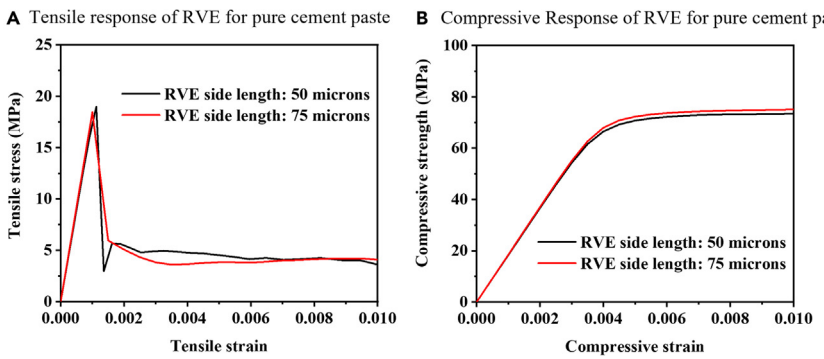

Figure 6. Mechanical responses of the RVE models for pure cement paste under the strain rate of 0.1/s

(A) The tensile responses of the RVE models with the side length of 50 and 75 μm.

(B) The compressive responses of the RVE models with the side length of 50 and 75 μm.

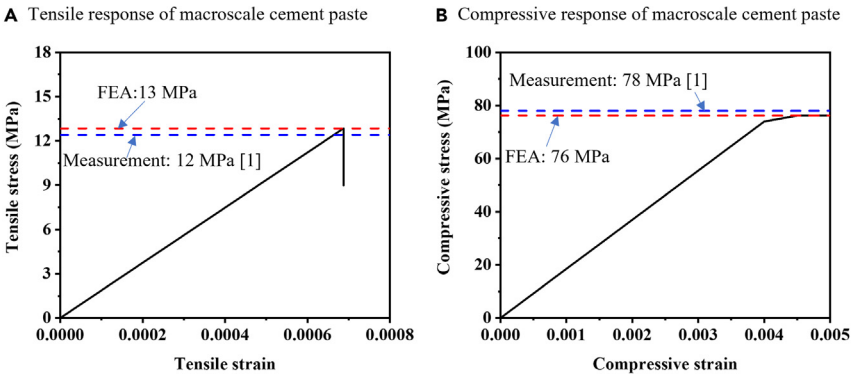

Figure 7. Mechanical responses of pure cement paste from FEA and the strength from FEA and measurement

(A) The tensile responses and the tensile strength.

(B) The compressive response and the compressive strength.

FEA. By adopting different levels of strain rates, the FEA shows that the strain rate changing from 0.1/s to 0.01/s has limited influence on the tensile strength and the compressive strength. Specifically, the tensile strength of the RVE model is 19 MPa, with the strain rate changing from 0.1/s to 0.01/s, as shown in Figure 5A. The compressive strength of the RVE model changes from 73.4 to 67.4 MPa, with the strain rate changing from 0.1/s to 0.01/s, as shown in Figure 5B. The FEA results in Figure 5 indicate that the strain rates of 0.1/s and 0.01/s have limited influence on the tensile strength and the compressive strength of the RVE model. Hence, the strain rate of 0.1/s is adopted in this study. To determine the sizes of the RVE model, three RVE models with different side lengths are deformed under tensile and compressive loadings at the strain rate of 0.1/s, respectively. The FEA shows that the size of the RVE model has limited influence on the tensile strength. Specifically, the tensile strengths are 19 and 18.5 MPa for the side lengths of the RVE models of 50 and 75 μm, respectively, as shown in Figure 6A. The compressive strengths of the RVE model are 73.3 and 75.2 MPa for the side lengths of the RVE models of 50 and 75 μm, respectively, as shown in Figure 6B. The FEA results in Figure 6 indicate that the side lengths of 50 and 75 μm have limited influence on the tensile strength and the compressive strength of the RVE model. Hence, the simulation results of the RVE model with a side length of 50 μm are adopted to simulate the macroscale cement paste in the FEA.

Based on the RVE model, the tensile strength and compressive strength are obtained. Afterward, the cohesion and the frictional angle are calculated through the Mohr-Coulomb model, which associates the uniaxial tensile strength and the uniaxial compressive strength with the cohesion and frictional angle given by[64]

$$\begin{cases} f_t = \dfrac{2c\cos\varphi}{1+\sin\varphi} \\ f_c = \dfrac{2c\cos\varphi}{1-\sin\varphi} \end{cases} \quad \text{(Equation 3)}$$

where f_t is the tensile strength; f_c is the compressive strength; c is the cohesion; and φ is the internal frictional angle. The

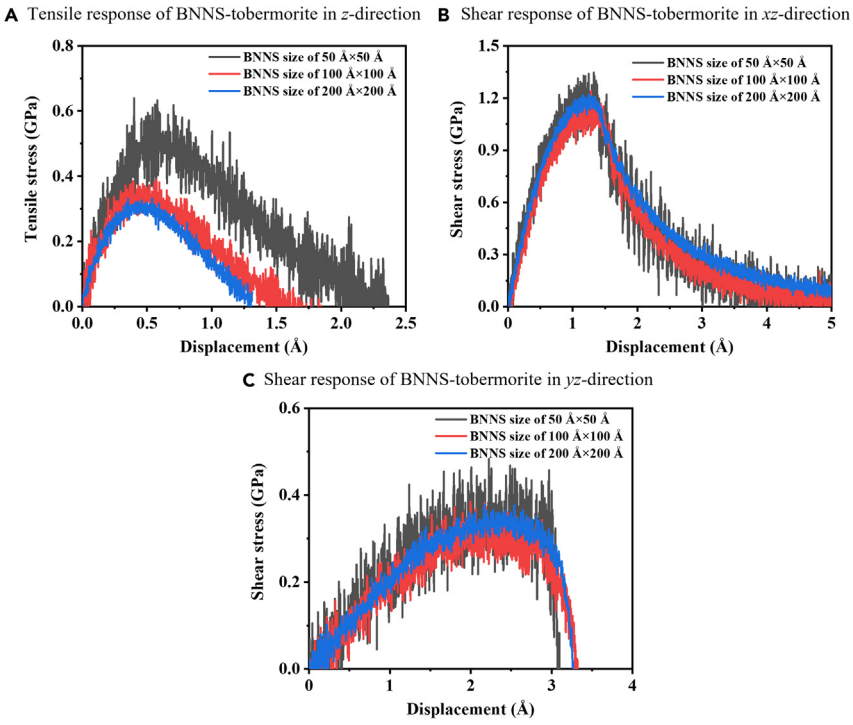

Figure 8. MD-based traction-separation relation at the BNNS-tobermorite interface for different sizes of BNNSs

(A) Variation of tensile stress with tensile displacement in the *z* direction for different sizes of BNNSs.

(B) Variation of shear stress with shear displacement in the *xz* direction for different sizes of BNNSs.

(C) Variation of shear stress with shear displacement in the *yz* direction for different sizes of BNNSs.

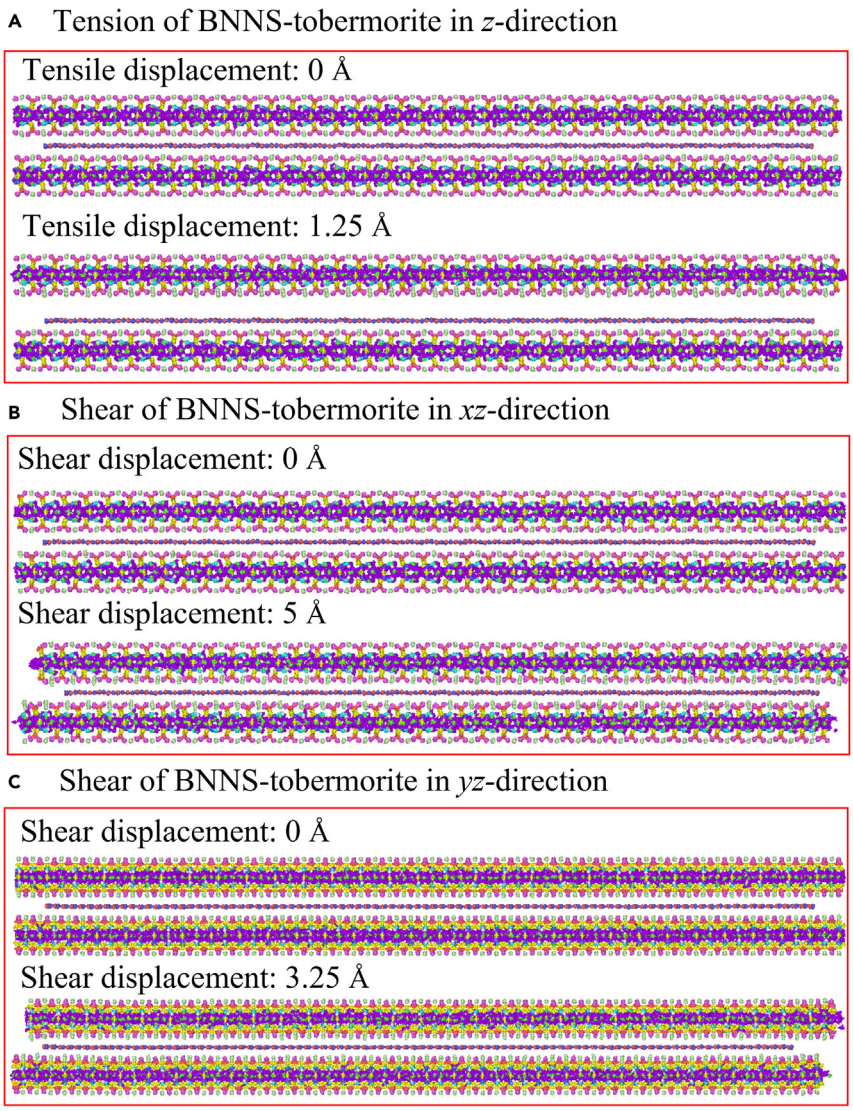

Figure 9. The deformation of BNNS-reinforced tobermorite with BNNS sizes of 200 × 200 Å and with tobermorite sizes of 214 × 214.2 × 26.5 Å

(A) The tensile deformation behavior in the *z* direction at the tensile displacement of 0 Å and 1.25 Å.
(B) The shear deformation behavior in the *xz* direction at the shear displacement of 0 Å and 5 Å.
(C) The shear deformation behavior in the *yz* direction at the shear displacement of 0 Å and 3.25 Å.

mechanical properties of the RVE model are taken as the input parameters for simulating the mechanical properties of the macroscale cement paste. Hence, the tensile response and the compressive response of the macroscale cement paste are obtained in the FEA, as shown in Figure 7. The tensile strength and the compressive strength values of 13 and 76 MPa are close to the measurements of 12 and 78 MPa in previous research, respectively.[1] The consistency of the finite element simulation results and the measurements indicates that the RVE model and the corresponding material parameters for simulating the macroscale cement paste are appropriate. With the validation of the prediction of the tensile strength and the compressive strength of the cement paste, we can adopt the Mohr-Coulomb model to describe the cement paste in BNNS-reinforced cement paste composite.

MD-based traction-separation relation

It is validated that the tensile strength and compressive strength of cement paste are accurately predicted by the multiscale modeling in this study. Hence, the accuracy of the prediction of the tensile strength and the compressive strength of BNNS-reinforced cement paste in the FEA is dependent on the interfacial cohesive properties between BNNSs and cement paste. The interfacial cohesive properties between BNNSs and cement paste are studied by MD simulations. To avoid the influence of the sizes of BNNSs on the interfacial cohesive properties between BNNSs and tobermorite (representing cement paste), the sizes of the atomistic models are changed. The sizes of the BNNSs range from 50 × 50 and 100 × 100 to 200 × 200 Å. The coresponding sizes of the tobermorite are 56.3 × 58.8 × 26.5, 112.6 × 110.8 × 26.5, and 214 × 214.2 × 26.5 Å. The traction-separation relation for the BNNS-tobermorite system with different sizes is shown in Figure 8. It indicates that the size variation of BNNSs has limited influence on the traction-separation relation between BNNSs and tobermorite in the z direction and the xz direction, which are shown in Figures 8A and 8B, respectively. In the yz direction, the traction-separation relation between BNNSs and tobermorite fluctuates drastically for BNNSs with sizes of 50 × 50 Å and tobermorite with sizes of 56.3 × 58.8 × 26.5 Å. For the larger sizes of the BNNS-tobermorite composite, the traction-separation relations are close and stable in the yz direction, as shown in Figure 8C. Hence, the traction-separation relation between BNNSs and tobermorite obtained from BNNSs with sizes of 200 × 200 Å and tobermorite with sizes of 214 × 214.2 × 26.5 Å is adopted in the FEA. The deformation behaviors of the BNNS-tobermorite composite under tensile and shear loadings are shown in Figure 9. The tensile loading in the z direction results in the interfacial peeling between BNNSs and tobermorite. The traction force transferred at the BNNS-tobermorite interface varies with the peeling distance in the z direction, as shown in Figure 9A. Under shear loadings in the xz direction and the yz direction, the BNNS-tobermorite interface is damaged due to the interfacial sliding. The traction forces varying with the interfacial

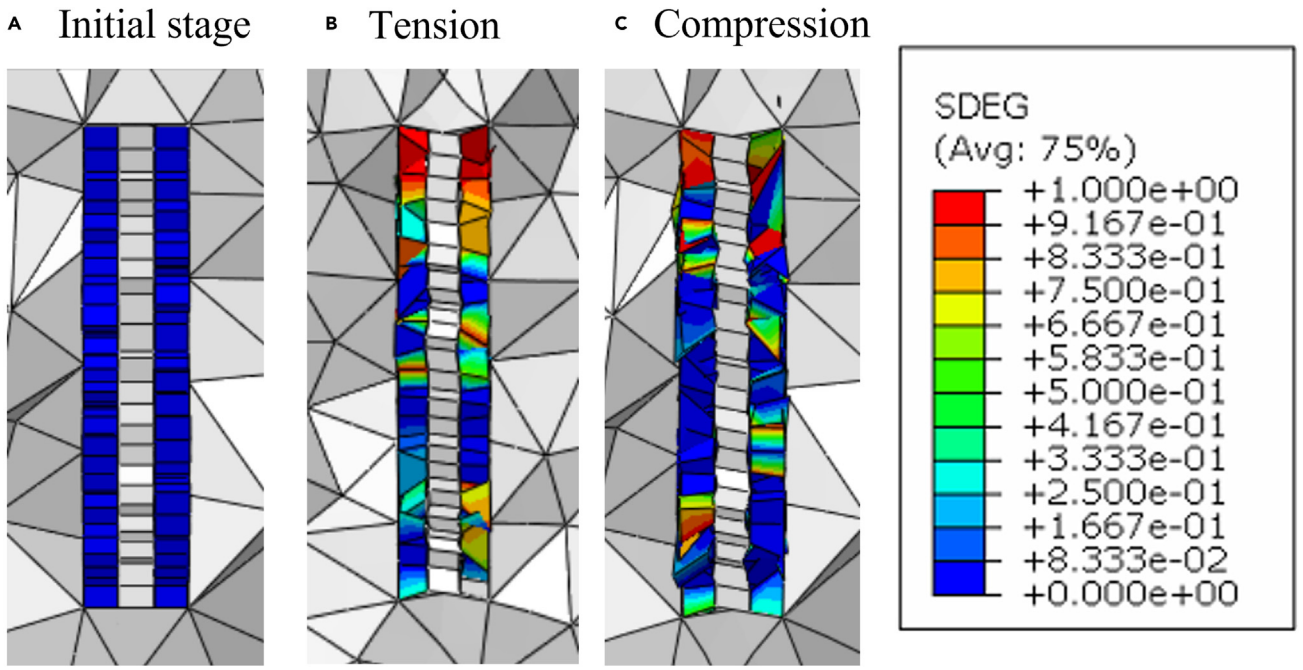

Figure 10. The scalar stiffness degradation (SDGE) of the interface between BNNSs and cement paste

(A) At the initial stage.

(B) Under tension.

(C) Under compression.

displacements are shown in Figure 9B under the xz-direction loading and in Figure 9C under the yz-direction loading. Based on the tensile test and shear tests through MD simulations, the cohesive properties at the discontinuous interface between BNNSs and tobermorite are quantified. The stress transfer at the interface between BNNSs and cement paste can be described by these cohesive properties in the FEA.

Validation of MD-based cohesive zone model

The simulation results of different sizes of pure mesoscale cement paste indicate that the results are insensitive to the sizes of the RVE model at mesoscale, as shown in Figure 6. Hence, the side length of the RVE-1 model is 0.285 μm to ensure that the weight fraction of BNNSs is 0.003% and that BNNSs with the average diameter of ~0.1 μm can be included in the RVE-1 model. The interface between BNNSs and cement paste is described by cohesive elements. The damage initiation criterion of the cohesive element is given by[65]

$$MAX\left\{\frac{\langle \varepsilon_n \rangle}{\varepsilon_b^{max}}, \frac{\varepsilon_s}{\varepsilon_s^{max}}, \frac{\varepsilon_t}{\varepsilon_t^{max}}\right\} = 1 \qquad \text{(Equation 4)}$$

where ε_n and ε_b^{max} are the nominal stress and the strength in the pure normal mode, respectively; ε_s and ε_s^{max} are the nominal stress and strength in the first shear direction, respectively; and ε_t and ε_t^{max} are the nominal stress and strength in the second shear direction, respectively. These parameters can be obtained from the MD-based cohesive zone model, as shown in Figure 8. The damage evolution of the cohesive elements is described by the power law[65]

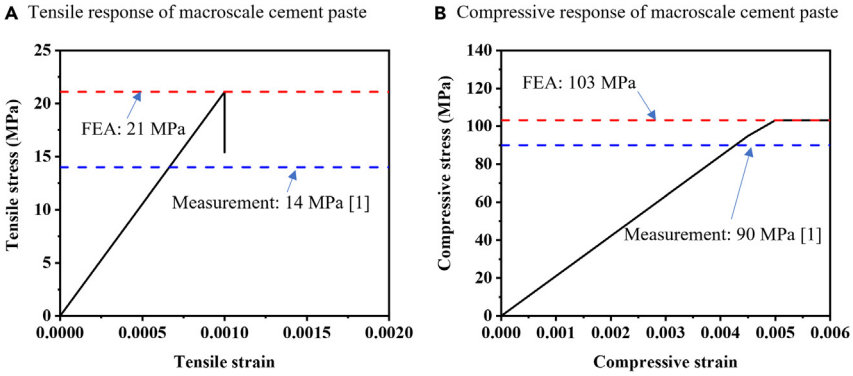

Figure 11. Mechanical responses and strength of BNNS-reinforced cement paste from FEA and the strength from FEA and measurement

(A) The tensile responses and the tensile strength.

(B) The compressive response and the compressive strength.

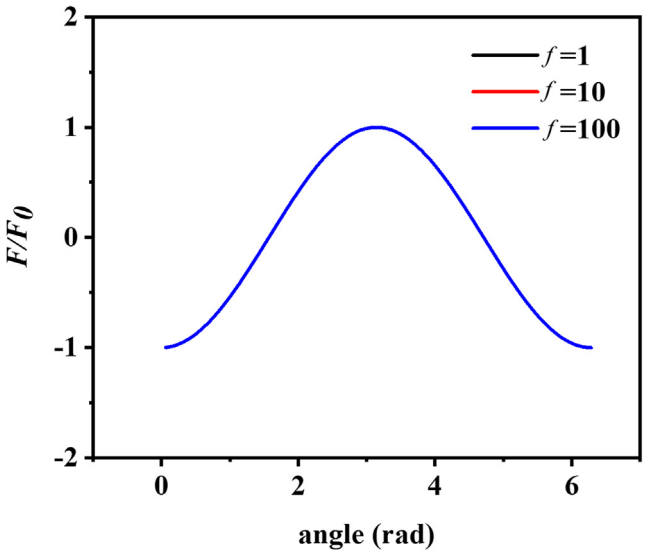

Figure 12. The relation between the transferred load and the inclined angle for different values of coefficient *f*

$$\left(\frac{G_I}{G_{Ic}}\right)^{\alpha} + \left(\frac{G_{II}}{G_{IIc}}\right)^{\alpha} + \left(\frac{G_{III}}{G_{IIIc}}\right)^{\alpha} = 1 \qquad \text{(Equation 5)}$$

where G_{Ic} is the normal mode fracture energy; G_{IIc} is the shear mode fracture energy's first direction; and G_{IIIc} is the shear mode fracture energy's second direction. These parameters can be obtained from the MD-based cohesive zone model, as shown in Figure 8. α is the power of the energetic criterion. The linear energetic criterion with $\alpha = 1$ and the quadratic energetic criterion with $\alpha = 2$ are the most used. In this study, the linear energetic criterion is adopted.

Under tensile and compressive loadings with a strain rate of 0.1/s, the interface between BNNSs and cement paste is damaged. Figure 10 shows the scaler stiffness degradation (SDGE) of cohesive elements that are used to describe the interfacial cohesive properties between BNNSs and cement paste. The red color indicates that the cohesive element is totally damaged. The SDGE is equal to one. The blue color indicates that the cohesive element is not damaged. The SDGE is equal to zero. For other colors, the SDGE value is large than zero and less than one, which indicates that the damage of the cohesive element begins. To validate the cohesive zone model used to describe the interface between BNNSs and cement paste, the material properties of the RVE-1 model as the input parameters are adopted to describe the mechanical behavior of the RVE-2 model, as shown in Figures 2E and 2F. In view of the tensile strength and compressive strength of the pure cement paste being insensitive to the side length of the RVE models, as shown in Figure 5, the side lengths of the RVE-1 model and the RVE-2 model are set to 0.285 and 10 μm in the FEA, respectively. The material properties of the RVE-2 model are used to describe the mechanical behavior of the macroscale cement paste in the FEA, as shown in Figure 2G. The mechanical properties of the macroscale cement paste in the FEA are dependent on the cohesive properties at the interface between BNNSs and cement paste. Hence, the MD-based cohesive zone model is validated by comparing the tensile strength and compressive strength of the macroscale cement paste from the FEA with that from measurements. Figure 11 shows the tensile strength and compressive strength of the macroscale cement paste obtained from the FEA and measurements. The tensile strengths of the macroscale cement paste from the FEA and the measurements are 21 and 14 MPa, respectively, as shown in Figure 11A. The compressive strengths of the macroscale cement paste from the FEA and the measurements are 103 and 90 MPa, respectively, as shown in Figure 11B. The discrepancy between the FEA and measurement is attributed to the pore size distribution in cement paste. In the FEA, the average sizes of the pores are adopted, which can affect the accuracy of the prediction in the tensile strength and the compressive strength. For the tensile strength in Figure 11A, the FEA result is larger than the measurement. This is due to the loading direction being parallel to the surface of BNNSs. The load transfer at the BNNS-tobermorite interface through the inclined BNNSs is given by[66]

$$F = F_0\left(e^{f\theta} - \cos\theta\right) \qquad \text{(Equation 6)}$$

where F_0 is the average internal force applied on the inclined BNNSs at a certain angle θ. f is the coefficient determined by experiments. From the Equation 6, the relation between the transferred load and the inclined angle is obtained, as shown in Figure 12. For different values of coefficient f, the maximum transferred load occurs at the inclined angle of $\theta = \pi$, which indicates that the tensile strength of BNNS-reinforced cementitious composite from FEA is the largest value because the angle between BNNSs and the loading direction is π. That is why the tensile strength in Figure 11A from FEA shows a discrepancy with that from measurements. To have a more accurate prediction of the tensile strength by FEA, the alignment of BNNSs needs to be captured so that the finite element model can accurately mimic the geometric characteristics of BNNS-reinforced cementitious composites. This issue can be addressed by measuring the pore size distributions from nanoscale to microscale and creating the corresponding models in the multiscale simulations.[67] Besides, the orientation of BNNSs in cement paste also have significant influence on the mechanical properties of cementitious composites, especially for the tensile strength.[66] To improve the accuracy of FEA for predicting the tensile strength and compressive strength, the alignment of BNNSs in cement paste can be modeled in FEA. By more accurately describing the geometry (e.g., pore size distribution and the alignment of BNNSs) of cementitious composites, the accuracy of the FEA results can be significantly improved.

Conclusion

In this article, the multiscale models of BNNS-reinforced cement paste are constructed to predict their tensile strength and compressive strength. In the multiscale models, the hierarchical RVE models are constructed to mimic the BNNS-reinforced cement paste at the microscale. The Mohr-Coulomb model is adopted to describe the mechanical behavior of the cement paste, which is validated by accurately predicting the tensile strength and the compressive strength of pure cement paste. The strain rate of

0.1/s is adopted to perform the tensile and the compressive tests in the FEA. By changing the sizes of the RVE model, it shows that the tensile strength and the compressive strength are insensitive to the size variations at the microscale. The equivalent shell element is adopted to describe the mechanical behavior of BNNSs, which is validated by previous research. MD simulations are performed to develop the cohesive zone model for describing the interface between BNNSs and cement paste. By changing the sizes of BNNSs, the convergenced traction-separation relation between BNNS and cement paste is obtained under the tensile loading and shear loadings. The traction-separation relation is invoked in the FEA, which yields the mechanical properties of the RVE models. Finally, the material properties of the RVE models are used to predict the tensile strength and compressive strength of the macroscale cement paste by the FEA, presenting very close tensile strength and compressive strength to that from the measurements.

EXPERIMENTAL PROCEDURES

Resource availability

Lead contact

Further information and requests for resources should be directed to and will be fulfilled by the lead contact, Denvid Lau (denvid.lau@cityu.edu.hk).

Materials availability

This study did not generate any new reagents or materials.

Data and code availability

The data and code and any additional information required to reanalyze the data reported in this paper are available from the lead contact upon request.

ACKNOWLEDGMENTS

The authors are grateful for the support from the Research Grants Council (RGC) of the Hong Kong Special Administrative Region, China (project no. 11213022), and City University of Hong Kong through an Applied Research Grant (project no. 9667236).

AUTHOR CONTRIBUTIONS

Conceptualization, J.L., W.L., C.L.C., and D.L.; data curation, J.L.; formal analysis, J.L.; investigation, J.L., C.L.C., and D.L.; methodology, J.L., W.L., C.L.C., and D.L.; software, J.L. and W.L.; visualization, J.L., W.L.; writing – original draft, J.L. and D.L.; writing – review & editing, J.L., W.L., C.L.C., and D.L.; funding acquisition, C.L.C. and D.L.; project administration, C.L.C. and D.L.; resources, C.L.C. and D.L.; supervision, D.L.

DECLARATION OF INTERESTS

The authors declare no competing interests.

Received: November 12, 2022
Revised: January 12, 2023
Accepted: March 9, 2023
Published: April 7, 2023

REFERENCES

1. Wang, W., Chen, S.J., Basquiroto de Souza, F., Wu, B., and Duan, W.H. (2018). Exfoliation and dispersion of boron nitride nanosheets to enhance ordinary Portland cement paste. Nanoscale *10*, 1004–1014.
2. Rafiee, M.A., Narayanan, T.N., Hashim, D.P., Sakhavand, N., Shahsavari, R., Vajtai, R., and Ajayan, P.M. (2013). Hexagonal boron nitride and graphite oxide reinforced multifunctional porous cement composites. Adv. Funct. Mater. *23*, 5624–5630.
3. Liu, J., Hui, D., and Lau, D. (2022). Two-dimensional nanomaterial-based polymer composites: fundamentals and applications. Nanotechnol. Rev. *11*, 770–792.
4. Jiang, X.-F., Weng, Q., Wang, X.-B., Li, X., Zhang, J., Golberg, D., and Bando, Y. (2015). Recent progress on fabrications and applications of boron nitride nanomaterials: a review. J. Mater. Sci. Technol. *31*, 589–598.
5. Weng, Q., Wang, X., Wang, X., Bando, Y., and Golberg, D. (2016). Functionalized hexagonal boron nitride nanomaterials: emerging properties and applications. Chem. Soc. Rev. *45*, 3989–4012.
6. Yang, H., Cui, H., Tang, W., Li, Z., Han, N., and Xing, F. (2017). A critical review on research progress of graphene/cement based composites. Compos. Appl. Sci. Manuf. *102*, 273–296.
7. Liu, J., Jian, W., and Lau, D. (2022). Boron nitride nanosheet as a promising reinforcement for cementitious composites. Appl. Surf. Sci. *572*, 151395.
8. Mayo, S.L., Olafson, B.D., and Goddard, W.A. (1990). DREIDING: a generic force field for molecular simulations. J. Phys. Chem. *94*, 8897–8909.
9. (2018). Chapter 13-Advanced and low cost energy and lighting devices. In Fundamentals and Applications of Nano Silicon in Plasmonics and Fullerines, M. Nayfeh, ed. (Elsevier), pp. 363–429.
10. Lau, D., Büyüköztürk, O., and Buehler, M.J. (2012). Characterization of the intrinsic strength between epoxy and silica using a multiscale approach. J. Mater. Res. *27*, 1787–1796.
11. Papadopoulos, V., Seventekidis, P., and Sotiropoulos, G. (2017). Stochastic multiscale modeling of graphene reinforced composites. Eng. Struct. *145*, 176–189.
12. Liu, J., Liu, J., Mei, J., and Huang, W. (2018). Investigation on manufacturing and mechanical behavior of all-composite sandwich structure with Y-shaped cores. Compos. Sci. Technol. *159*, 87–102.
13. Papadopoulos, V., and Impraimakis, M. (2017). Multiscale modeling of carbon nanotube reinforced concrete. Compos. Struct. *182*, 251–260.
14. Bargmann, S., Klusemann, B., Markmann, J., Schnabel, J.E., Schneider, K., Soyarslan, C., and Wilmers, J. (2018). Generation of 3D representative volume elements for heterogeneous materials: a review. Prog. Mater. Sci. *96*, 322–384.
15. Cui, K., Chang, J., Feo, L., Chow, C.L., and Lau, D. (2022). Developments and applications of carbon nanotube reinforced cement-based composites as functional building materials. Front. Mater. *9*, 861646.
16. Aboudi, J., Arnold, S.M., and Bednarcyk, B.A. (2013). Micromechanics of Composite Materials: A Generalized Multiscale Analysis Approach (Butterworth-Heinemann).
17. Chandra, Y., Adhikari, S., Saavedra Flores, E.I., and Figiel, Ł. (2020). Advances in finite element modelling of graphene and associated nanostructures. Mater. Sci. Eng. R Rep. *140*, 100544.
18. Lu, X., and Hu, Z. (2012). Mechanical property evaluation of single-walled carbon nanotubes by finite element modeling. Compos. B Eng. *43*, 1902–1913.
19. Georgantzinos, S., Kariotis, K., Giannopoulos, G., and Anifantis, N. (2020). Mechanical properties of hexagonal boron nitride monolayers: finite element and analytical predictions. Proc. IME C J. Mech. Eng. Sci. *234*, 4126–4135.
20. Rafiee, R., and Eskandariyun, A. (2017). Comparative study on predicting Young's modulus of graphene sheets using nano-scale continuum mechanics approach. Phys. E Low-dimens. Syst. Nanostruct. *90*, 42–48.
21. Giannopoulos, G.I., Kakavas, P.A., and Anifantis, N.K. (2008). Evaluation of the effective mechanical properties of single walled carbon nanotubes using a spring based finite element approach. Comput. Mater. Sci. *41*, 561–569.
22. BabuA, R., Benipal, G.S., and Singh, A.K. (2005). Constitutive modelling of concrete: an overview. Asian J. Civ. Eng. *6*, 211–246.
23. Xie, S.Y., Shao, J.F., and Burlion, N. (2008). Experimental study of mechanical behaviour of cement paste under compressive stress and chemical degradation. Cem. Concr. Res. *38*, 1416–1423.

24. Sarikaya, A., and Erkmen, R.E. (2019). A plastic-damage model for concrete under compression. Int. J. Mech. Sci. *150*, 584–593.

25. Binder, E., Reihsner, R., Yuan, Y., Mang, H.A., and Pichler, B.L.A. (2020). High-dynamic compressive and tensile strength of specimens made of cementitious materials. Cem. Concr. Res. *129*, 105890.

26. Fischer, I., Pichler, B., Lach, E., Terner, C., Barraud, E., and Britz, F. (2014). Compressive strength of cement paste as a function of loading rate: experiments and engineering mechanics analysis. Cem. Concr. Res. *58*, 186–200.

27. Palkovic, S.D., and Büyüköztürk, O. (2018). Multiscale modeling of cohesive-frictional strength properties in cementitious materials. In Handbook of Materials Modeling: Applications: Current and Emerging Materials, W. Andreoni and S. Yip, eds. (Springer International Publishing), pp. 1–24.

28. Wang, X., Zhang, M., and Jivkov, A.P. (2016). Computational technology for analysis of 3D meso-structure effects on damage and failure of concrete. Int. J. Solid Struct. *80*, 310–333.

29. Elices, M., Guinea, G.V., Gómez, J., and Planas, J. (2002). The cohesive zone model: advantages, limitations and challenges. Eng. Fract. Mech. *69*, 137–163.

30. Zavattieri, P.D., Raghuram, P.V., and Espinosa, H.D. (2001). A computational model of ceramic microstructures subjected to multi-axial dynamic loading. J. Mech. Phys. Solid. *49*, 27–68.

31. Sazgar, A., Movahhedy, M.R., Mahnama, M., and Sohrabpour, S. (2017). Development of a molecular dynamic based cohesive zone model for prediction of an equivalent material behavior for Al/Al2O3 composite. Mater. Sci. Eng. A *679*, 116–122.

32. Gall, K., Horstemeyer, M.F., Van Schilfgaarde, M., and Baskes, M.I. (2000). Atomistic simulations on the tensile debonding of an aluminum–silicon interface. J. Mech. Phys. Solid. *48*, 2183–2212.

33. Dandekar, C.R., and Shin, Y.C. (2011). Molecular dynamics based cohesive zone law for describing Al–SiC interface mechanics. Compos. Appl. Sci. Manuf. *42*, 355–363.

34. Elkhateeb, M.G., and Shin, Y.C. (2018). Molecular dynamics-based cohesive zone representation of Ti6Al4V/TiC composite interface. Mater. Des. *155*, 161–169.

35. Gupta, P., Pal, S., and Yedla, N. (2016). Molecular dynamics based cohesive zone modeling of Al (metal)–Cu50Zr50 (metallic glass) interfacial mechanical behavior and investigation of dissipative mechanisms. Mater. Des. *105*, 41–50.

36. Pellenq, R.J.M., Kushima, A., Shahsavari, R., Van Vliet, K.J., Buehler, M.J., Yip, S., and Ulm, F.-J. (2009). A realistic molecular model of cement hydrates. Proc. Natl. Acad. Sci. USA *106*, 16102–16107.

37. Abdolhosseini Qomi, M.J., Krakowiak, K.J., Bauchy, M., Stewart, K.L., Shahsavari, R., Jagannathan, D., Brommer, D.B., Baronnet, A., Buehler, M.J., Yip, S., et al. (2014). Combinatorial molecular optimization of cement hydrates. Nat. Commun. *5*, 4960.

38. Hou, D., Zhu, Y., Lu, Y., and Li, Z. (2014). Mechanical properties of calcium silicate hydrate (C–S–H) at nano-scale: a molecular dynamics study. Mater. Chem. Phys. *146*, 503–511.

39. Basquiroto de Souza, F., Shamsaei, E., Chen, S., Sagoe-Crentsil, K., and Duan, W. (2021). Controlled growth and ordering of poorly-crystalline calcium-silicate-hydrate nanosheets. Commun. Mater. *2*, 84.

40. Liu, J., Hu, N., Chow, C.L., and Lau, D. (2022). Unfolding behavior of self-folded boron nitride nanosheets inducing ductility of cementitious composites. Appl. Surf. Sci. *599*, 153818.

41. Mishra, R.K., Mohamed, A.K., Geissbühler, D., Manzano, H., Jamil, T., Shahsavari, R., Kalinichev, A.G., Galmarini, S., Tao, L., Heinz, H., et al. (2017). cemff: a force field database for cementitious materials including validations, applications and opportunities. Cem. Concr. Res. *102*, 68–89.

42. Shahsavari, R., Buehler, M.J., Pellenq, R.J.M., and Ulm, F.-J. (2009). First-principles study of elastic constants and interlayer interactions of complex hydrated oxides: case study of tobermorite and jennite. J. Am. Ceram. Soc. *92*, 2323–2330.

43. Moon, W.H., and Hwang, H.J. (2004). Molecular-dynamics simulation of defect formation energy in boron nitride nanotubes. Phys. Lett. *320*, 446–451.

44. Moon, W.H., and Hwang, H.J. (2004). Molecular-dynamics simulation of structure and thermal behaviour of boron nitride nanotubes. Nanotechnology *15*, 431–434.

45. Bu, H., Zheng, H., Zhou, H., Zhang, H., Yang, Z., Liu, Z., Wang, H., and Xu, Q. (2019). The role of sp^2 and sp^3 hybridized bonds on the structural, mechanical, and electronic properties in a hard BN framework. RSC Adv. *9*, 2657–2665.

46. Mukhopadhyay, T.K., and Datta, A. (2017). Deciphering the role of solvents in the liquid phase exfoliation of hexagonal boron nitride: a molecular dynamics simulation study. J. Phys. Chem. C *121*, 811–822.

47. Zhao, L., Guo, X., Ge, C., Li, Q., Guo, L., Shu, X., and Liu, J. (2017). Mechanical behavior and toughening mechanism of polycarboxylate superplasticizer modified graphene oxide reinforced cement composites. Compos. B Eng. *113*, 308–316.

48. Shahsavari, R. (2018). Intercalated hexagonal boron nitride/silicates as bilayer multifunctional ceramics. ACS Appl. Mater. Interfaces *10*, 2203–2209.

49. Akıner, T., Mason, J.K., and Ertürk, H. (2016). A new interlayer potential for hexagonal boron nitride. J. Phys. Condens. Matter *28*, 385401.

50. Plimpton, S. (1995). Fast parallel algorithms for short-range molecular dynamics. J. Comput. Phys. *117*, 1–19.

51. Zhou, J., and Liang, Y. (2019). Effect of water on the dynamic tensile mechanical properties of calcium silicate hydrate: based on molecular dynamics simulation. Materials *12*, 2837.

52. Zhang, N., and Chen, Y. (2013). Nanoscale plastic deformation mechanism in single crystal aragonite. J. Mater. Sci. *48*, 785–796. https://doi.org/10.1007/s10853-012-6796-1.

53. Zhang, N., Carrez, P., and Shahsavari, R. (2017). Screw-dislocation-induced strengthening–toughening mechanisms in complex layered materials: the case study of tobermorite. ACS Appl. Mater. Interfaces *9*, 1496–1506.

54. Omairey, S.L., Dunning, P.D., and Sriramula, S. (2019). Development of an ABAQUS plugin tool for periodic RVE homogenisation. Eng. Comput. *35*, 567–577.

55. Constantinides, G. (2002). The Elastic Properties of Calcium Leached Cement Pastes and Mortars: A Multi-Scale Investigation (Massachusetts Institute of Technology).

56. Yu, Z., Zhou, A., and Lau, D. (2016). Mesoscopic packing of disk-like building blocks in calcium silicate hydrate. Sci. Rep. *6*, 36967.

57. Wells, G.N., and Sluys, L.J. (2001). Three-dimensional embedded discontinuity model for brittle fracture. Int. J. Solid. Struct. *38*, 897–913.

58. Liu, W.-H., Zhang, L.-W., and Liew, K.M. (2020). Modeling of crack bridging and failure in heterogeneous composite materials: a damage-plastic multiphase model. J. Mech. Phys. Solid. *143*, 104072.

59. Hou, Y., and Wang, L. (2017). Multiscale mechanical modeling of hydrated cement paste under tensile load using the combined DEM-MD method. Front. Struct. Civ. Eng. *11*, 270–278.

60. Sarris, E., and Constantinides, G. (2013). Finite element modeling of nanoindentation on C–S–H: effect of pile-up and contact friction. Cem. Concr. Compos. *36*, 78–84.

61. Němeček, J., Králík, V., Šmilauer, V., Polívka, L., and Jäger, A. (2016). Tensile strength of hydrated cement paste phases assessed by micro-bending tests and nanoindentation. Cem. Concr. Compos. *73*, 164–173.

62. Hou, D., Lu, Z., Li, X., Ma, H., and Li, Z. (2017). Reactive molecular dynamics and experimental study of graphene-cement composites: structure, dynamics and reinforcement mechanisms. Carbon *115*, 188–208.

63. Abdelrahim, M.A.A., Elthakeb, A., Mohamed, U., and Noaman, M.T. (2021). Effect of steel fibers and temperature on the mechanical properties of reactive powder concrete. Civ. Environ. Eng. *17*, 270–276.

64. Bahmani, B., Abedi, R., and Clarke, P. (2019). A stochastic bulk damage model based on mohr-coulomb failure criterion for dynamic rock fracture. Appl. Sci. *9*, 830.

65. ABAQUS® Documentation (2009). Dassault Systèmes: Vélizy-Villacoublay.

66. Lu, C., and Leung, C.K. (2016). A new model for the cracking process and tensile ductility of Strain Hardening Cementitious Composites (SHCC). Cem. Concr. Res. *79*, 353–365.

67. Qin, R., Zhou, A., Yu, Z., Wang, Q., and Lau, D. (2021). Role of carbon nanotube in reinforcing cementitious materials: an experimental and coarse-grained molecular dynamics study. Cem. Concr. Res. *147*, 106517.